

Landslides (2023) 20:2545–2562  
 DOI 10.1007/s10346-023-02115-6  
 Received: 11 January 2023  
 Accepted: 3 July 2023  
 Published online: 17 August 2023  
 © The Author(s) 2023

Giovanni B Crosta · Giuseppe Dattola · Camilla Lanfranconi ·  
 Fabio V De Blasio  · Marco Malusà · Davide Bertolo



## Rockfalls, fragmentation, and dust clouds: analysis of the 2017 Pousset event (Northern Italy)

**Abstract** The process and dynamics of rock fragmentation during the collapse of rockfalls and rock avalanches is a poorly developed topic. The most severe fragmentation often leads to the formation of a rock dust that rises to form a cloud suspended in the air. The understanding of fragmentation processes is hampered by the environmental disturbances that alter the dust cloud deposit shortly after deposition. Here, we study the fragmentation of the October 2017 Pousset rockfall, detached from a NNE facing steep bedrock wall in the permafrost zone, that involved 8,300m<sup>3</sup> of metamorphic rock and fell about 800 m. The collapse generated large boulders which rolled downslope and a thick and large dust cloud. The source and deposit were investigated, and dust cloud material was sampled at different locations to reconstruct an exponential thickness distribution and perform grain size characterization. The fragmentation energy was estimated by integrating the spectrum of the grains assuming that the fragmentation energy is proportional to the generated area. The fragmentation energy was found to be about 0.4% of the initial potential energy. Most probable fragmentation points and block deposition areas were evaluated and positioned by means of the HyStone 3D rockfall simulator. Furthermore, we calculated the flow rate of the suspended powder generated by the fragmentation process and compared the results with observations available for the evolution of the phenomenon and the collected samples. The Pousset event, in its relatively simple dynamics, may be a good testing ground to address the current theories of rockfall and rock avalanche fragmentation and dust cloud behavior.

**Keywords** Rockfall · Dust cloud · Fragmentation · HyStone · Permafrost thawing

### Introduction

Rockfalls in high mountain environments have been reported more frequently and with more details in the last decades (Gruber et al. 2004; Gruber and Haerberli 2007; Ravelin et al. 2017). Permafrost thaw in steep bedrock walls is considered the main cause of periglacial rock wall failures. Ice-filled joints are common under bedrock permafrost conditions and continuous ice-coated failure surfaces are frequently observed at source areas just after rockfall release (Geertsema et al. 2006; Ravelin et al. 2017; Walter et al. 2020). Ice-filled joints can be extended and opened because of ice segregation and wedging, but also by percolating water during thawing. It has been shown in the literature that rockfalls of very different volumes can be associated to such processes and this requires action of different triggering factors or of the same factor acting over different time scales. Because of the high relief of these steep rock walls,

rockfalls and avalanches can undergo very high drops and consequently propagate over long distances.

Although rockfalls and rock avalanches are common occurrences in the mountainous environment, they still hold many enigmatic aspects, especially regarding the dynamics and energetics of the fragmentation processes from the large portions of initially intact rock to finely comminuted clasts of wide size spectrum. Some rockfalls consist of single isolated blocks traveling downslope and colliding through successive bounces with the terrain and rolling. In this case, the frequent collisions dissipate much energy, and the block will only be partially fragmented or undergo continuous chipping. It is not unusual to observe meter or even decameter-size blocks to roll for several tens of meters, practically intact. In contrast with these rockfalls, when the terrain is very steep, a block may accelerate in the gravity field in ballistic flight or free fall for a great height,  $H$ , without continuous interaction with the ground. It will so accumulate an energy  $E_0 = \rho gHV$  where  $\rho$  is the rock density and  $V$  its volume, which is released in one or few catastrophic impacts, and severe fragmentation will occur at each impact. The most extreme cases have been recently analyzed under the name of Extremely Energetic Rockfalls (EER, De Blasio et al. 2018). These EERs are events in which the following two criteria are both met: high specific energy released at once (or equivalently great unimpeded fall height) and high total energy (or equivalently large mass), like for example the Yosemite rock falls (Morrissey et al. 1999; Wiczeorek et al. 2007). Thus, an EER is a falling boulder traveling mostly along ballistic trajectories along which it acquires kinetic energy without, or with little, interaction with the terrain. According to the definition proposed by De Blasio et al. (2018), EER events have sufficiently high total energy (of the order of some tens of GJ) to generate large mobile dust clouds and fragments capable to impact large areas. Altogether, 23 major documented events have been reported by De Blasio et al. (2018) worldwide even though such phenomena are believed to be much more frequent. Furthermore, there is evidence that permafrost can influence the stability of rock and debris masses in high mountain areas and consequently the progressive effects of climate change at high elevations and the consequent increase in temperature lead to destabilization of steep rock slopes triggering rockfalls, slides, and avalanches (Ravelin et al. 2010, 2017; Phillips et al. 2017).

The dust cloud formation mechanisms in EERs is different from the process observed in rock avalanches, where the interaction with the terrain is more or less continuous for a long distance. Rock avalanches fragment both at their basal layers especially via crushing along dynamical force chains, and in the interior due to surface chipping of fragments off the surface of the colliding clasts. Many observers have reported the onset of a dust cloud created by

high-energy fragmentation of rock down to microns to millimeter size clasts in both EER and rock avalanches. In the most extreme cases, the dust cloud can initially be produced in a state of high velocity and create a shock wave perceived as a strong perturbation of the air (Wieczorek et al. 2000, 2002). Millimeter-sized clasts fired at such a high rate can exfoliate and debark vegetation and produce other local and structural damages (De Blasio et al. 2018). After this initial phase, the resulting dust cloud often travels as an accelerated suspension from the gravitational field along the valley flank. So far, little research has concentrated on the creation and further flow of dust clouds. Furthermore, the dust clouds deposited in the areas surrounding the event are often overlooked in the global deposition of the event.

In this work, we analyze the collapse of the Cima Pousset in the north-western Italian Alps (Val D'Aosta) in October 2017. The 8300 m<sup>3</sup> rockfall detached at about 3000 m a.s.l. well within the permanent permafrost conditions (Fig. 1) according to the Alpine Permafrost Index Map (Boeckli et al. 2012). It was not particularly large but yet quite energetic in terms of fall height. The runout of the main blocks reached a distance between 500 and 800 m. The initial collapse phase created numerous blocks each some cubic meters in volume, which rolled along the local slope maintaining high kinetic energy. At the end of their trajectory, blocks hit the eastern flank of the peak, disintegrating at once at the base of the cliff, producing a large dust cloud that coated the area from the slope to the main valley bottom and the opposite valley side. Hence, the identification of the events unfolding during the Pousset landslide permits a direct and controlled examination of many of the still enigmatic aspects of rock avalanche and rockfall dynamics.

In the following, we describe first the geology and meteo-climatic characteristics of the area, and the dynamics and the main deposit characteristics of the 2017 event. Then, we present our modeling study of the detailed rockfall trajectories after the initial collapse. Finally, we suggest a physical explanation for the dust cloud generated by these collisions in terms of grain size distribution, energy of fragmentation, propagation, and dust settling.

### The 2017 Pousset rockfall

In contrast to most rockfall and avalanche occurrences, which are usually examined after weathering has altered the site condition and posing a minimal attention for the dust cloud deposit, a visit to the Pousset site was planned immediately after the event. This allowed us to sample the rock dust deposit from different points considered less exposed to risk, before rain and wind could disperse and alter the deposits. In fact, no major meteorological events occurred between the collapse and our first field trip to the location. As mentioned above, De Blasio et al. (2018) defined Extremely Energetic Rockfalls (EER) as the rockfalls of large total energy falling from extreme heights, and little interaction with the terrain. The threshold values of the fall height and involved energy are somehow arbitrary, and have been set at 300 m and about 80 GJ, respectively. The Pousset event, with a full drop height of about 800 m and energy of ca. 170 GJ, was within the definition of an EER regarding the total fall height and energy. However, the Pousset rockfall cannot be considered an EER since the interactions with the terrain was continuous, which implied a gradual reduction of the initial block potential energy.

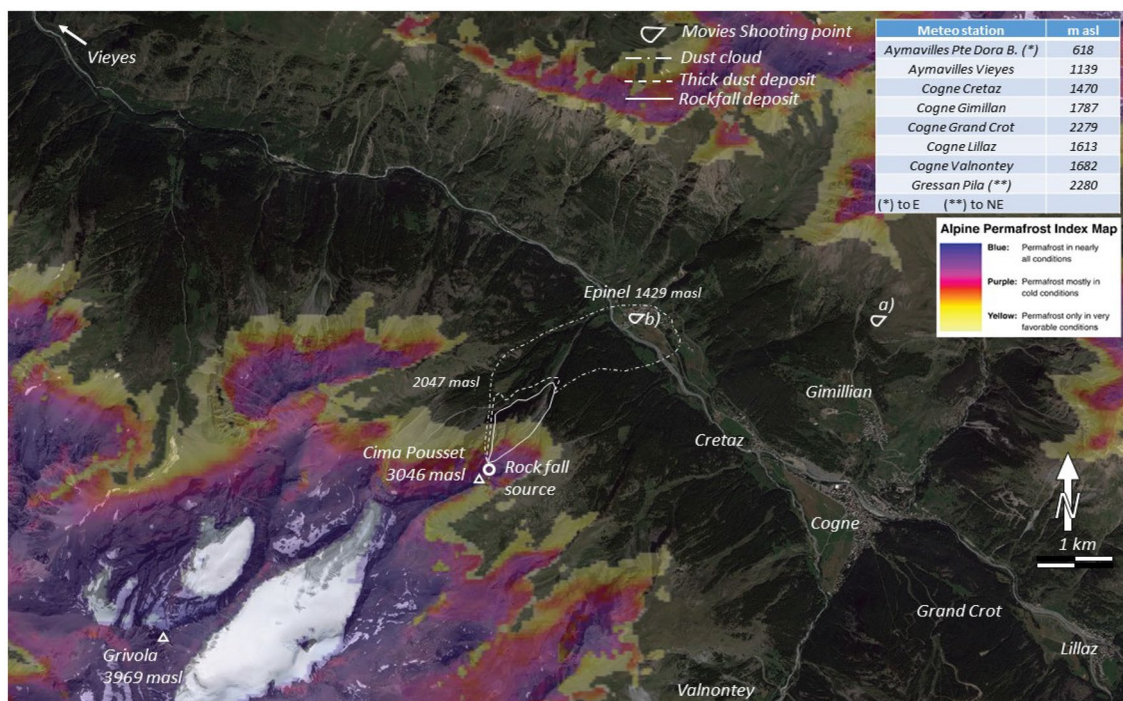


**Fig. 1** Location map of the area affected by the 2017 Pousset rockfall with position of the meteo-station and the deposits of the rockfall boulders and of the rock dusts. In colors are reported permafrost conditions according to the Alpine Permafrost Index Maps (Boeckli et al. 2012)

## Geological setting

The study area (Fig. 1) is located in the Penninic domain of the Italian Western Alps at the boundary between the so-called Eocene Eclogite Belt and the lower-grade Paleogene Frontal Wedge of the orogen (Malusà et al. 2015). The rockfall source area consists of serpentinites and metabasites of the Grivola-Urtier metaophiolitic Unit (Polino et al. 2015), which is part of the Eocene Eclogite Belt. These rocks underwent subduction to eclogite facies condition during the Cenozoic and were rapidly exhumed to the Earth's surface by the end of the Eocene, now forming a tectonic envelope on top of the eclogitic gneissic dome of the Gran Paradiso Massif. In the Cogne Valley, the Grivola-Urtier metaophiolites are juxtaposed against metamorphic rocks of the Frontal wedge by the Belleface-Trajo Fault, a steeply dipping ENE-WSW post-metamorphic fault that includes slivers of marbles, calcschists, and carbonate tectonic breccias (Malusà et al. 2005). This fault runs along the steep Trajo valley, representing the rockfall accumulation zone. On the north-western side of the fault are exposed Late Devonian meta-granodiorites (Bergomi et al. 2017) and associated country rocks of the Gran Nomenon Unit (Polino et al. 2015). These country rocks, which are part of the Frontal Wedge of the orogen, chiefly consist of albite-chlorite gneisses and experienced pre-Alpine metamorphism under epidote-amphibolite facies conditions followed by a greenschist facies Alpine overprint (Malusà et al. 2005). Serpentinites and metabasites of the rockfall source area show on average a main foliation dipping towards the NNE. This main foliation is cut by steep NE-dipping fault planes belonging to the Cogne Fault zone, a deformation zone including opposite-dipping fault segments that

exert a strong morphological control on the landscape as confirmed by the NW-SE trend of the Cogne Valley and Upper Aosta Valley. Based on available low-temperature thermochronology data, the Cogne fault was likely active during the mid-Miocene (Malusà et al. 2009). This tectonic arrangement controls the sliding mechanisms in the sub-vertical dip-slope source area.

## The 2017 event

The main event occurred on October 31 2017 at 12:17, and it was followed by a minor event at 12:43. Due to the time of the day and to the visibility from the valley bottom, it was recorded both on video and photo allowing for some detailed observations of the occurrence and of the associated effects. The Pousset (3046 m asl) is a sharp peak at the extremity of a thin NE trending ridge. The detachment occurred along a steeper part of the foliation about 80 m below the Pousset peak (Fig. 2a) along the NNE slope. Just after the event, a helicopter overflight allowed us to spot the presence of a centimeter- to decimeter-thick ice layer still attached along differently oriented sectors of the failure surface. The main fracture sets (K1, K2, and K3, see Fig. 2a) clearly define the geometry of the volume which detached from the cliff. The fracture sets isolated the roughly pyramidal failed block with a base and height estimated at about 500 m<sup>2</sup> and 50 m, respectively. The finding of ice on part of the detachment surface, delimited by the three sets, points to the hypothesis of water freezing and ice thawing along well-developed rock discontinuities as one of the triggering mechanisms. The surface of the ice layer, still pasted to the scar surface, was characterized by a series of wrinkles parallel to the discontinuity direction



**Fig. 2** Pousset peak (a) view with source area; the three main fracture sets controlling the detachment scar, the transit, and the deposits. Three areas with different block depositional characteristics are shown (D1, D2, and D3); (b) source area of the 8300 m<sup>3</sup> rockfall; (c) ice layer along the upper sector of the detachment plane; (d) tree cluster uprooted and covered by a thick dust layer; (e) upward view of the slope; (f) and (g) tree stumps and uprooted trees in the area of thick dust cloud and blocks propagation

(see Fig. 2c). Ice evidence was mainly visible in the upper part of the failure surface where the block was just a few meters thick. These observations support the idea that weakening by permafrost thawing and ice melting could occur prevalently at the base of the failing block, along the contact between block and ice, by heat conduction and secondarily by advection. In general, it is expected that the maximum active layer thickness is reached late in the year (October to December, Gruber and Haeblerli 2007) and the Pousset event seems to support this critical condition. In the case of the Pousset peak, the underground temperature distribution and regime are the result of the three-dimensional effects controlled by the narrow NE trending ridge, the consequent difference in spatial temperature distribution at the surface (SE, NW, and NE facing slopes (see Fig. 1), the seasonal transience of surface temperature, and also the thermo-physical anisotropy strongly controlled by the persistent foliation.

Following the initial detachment, a small dust cloud developed from the source area and along the steep cliff (see Fig. 3a) but it never developed noticeably with time whereas a much larger and rapidly moving cloud was generated when a large part of the falling blocks reached the base of the cliff. This main cloud infilled the tributary valley (Trajo valley; Fig. 3a and b), increasing in thickness and with its front moving against the opposite valley flank and then rapidly descending towards the main valley. In about 2 min after its formation, the main dust cloud reached the valley bottom climbing about 100 m on the opposite valley side and enlarging along the valley bottom (see the approximate cloud limits in Fig. 1). At this time, the Epinel village and the main valley road were obscured hampering visibility. Then, the cloud slowly evolved and stratified in air lasting for a total of circa 30 min. Assuming a total maximum fall height of 800 m (impact

velocity  $125 \text{ ms}^{-1}$ ) and an initial volume of  $8300 \text{ m}^3$  of rock (density  $2700 \text{ kg/m}^3$ ), the specific energy per unit mass results  $7848 \text{ J/kg}^{-1}$  and a total energy  $170 \text{ GJ}$ .

The trajectories of the falling blocks concentrated in the N and NE directions, the first one following a steeper path ending with a 250 m high vertical jump just before reaching the talus deposits, and the second one following a long slope controlled by the foliation planes (Fig. 2a and e). As a consequence, two main deposition zones were recognized (D1 and D2 in Fig. 5).

The temperature records for eight stations distributed around the rockfall area were examined to look for long-term and short-term changes. In the 2010–2022 period, a mean increase in temperature was recorded ranging between  $0.04$  and  $0.17 \text{ }^\circ\text{C/year}$  with a slight positive relationship with elevation (see Fig. 4a). The year 2017 was not anomalous with respect to the others in the time series (Fig. 4a and b). The mean daily temperature in the week before the event decreased by  $1.2$ – $1.6 \text{ }^\circ\text{C/day}$  from about  $8$ – $12$  to  $1$ – $4 \text{ }^\circ\text{C}$  (Fig. 4c) whereas no rainfall occurred close to the event (Fig. 4d). Following Paranunzio et al. (2016), we analyzed temperature data collected from weather stations in the proximity of the event. The analysis of the temperatures at the stations in Vieyes and Gimillian (Fig. 1) showed that the week before the rockfall was characterized by higher temperatures than those recorded in the 2010–2018 period. Analyzing the 30-day interval preceding the rockfall, it was found that at the Vieyes, Gimillian, and Grand Crot stations (Fig. 1), a positive anomaly was recorded. In fact, the 30 days preceding the rockfall were characterized by higher temperatures than those recorded in the 2010–2018 period. These results could indicate a relationship with the triggering of the event, but further investigation required to support this thesis is beyond the aims of this study.

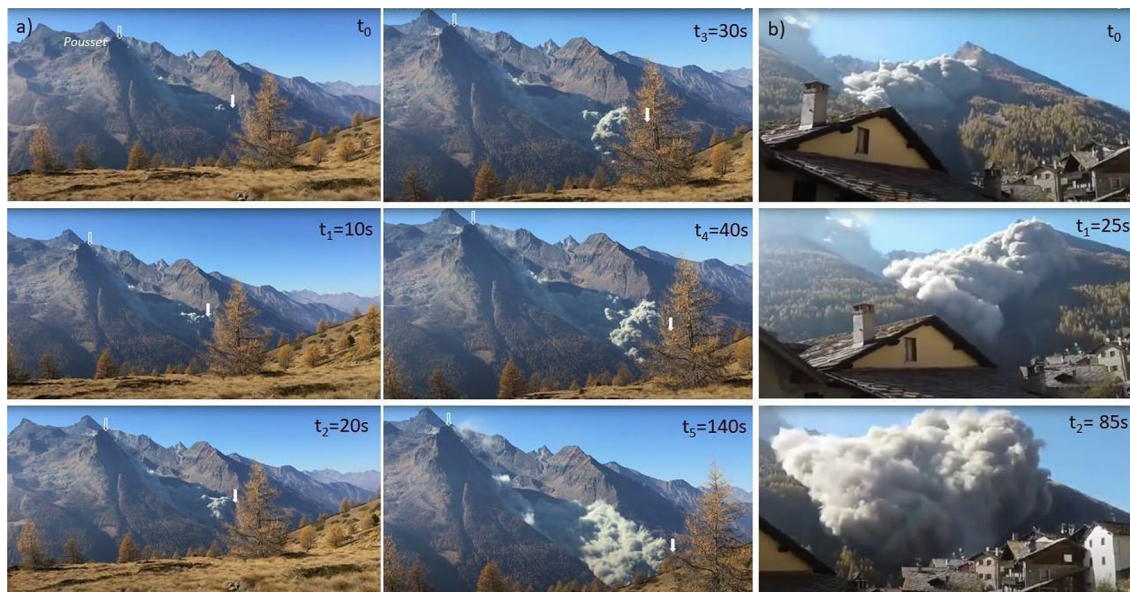


**Fig. 3** Propagation of the dust cloud from two videos recorded during the event (photo by I. Busto, see acknowledgements for the web link). The two shooting points are shown in Fig. 1 (a) from above Gimillian and (b) from the Epinel village. Time is from the initial time ( $t_0$ ) chosen for sequence. Sequence (a) show that the dust cloud in the source area and along the rocky cliff remains limited in extent during the entire falling time while it grows considerably along the gentler slope of tributary valley starting from a thickness of 50 to 100 m ( $t_0$  to  $t_1$  40 s in the video-sequence a). The cloud front at  $t_0$  in (b) reached about 300 m in thickness growing to about 500 m at  $t_2 = 85 \text{ s}$

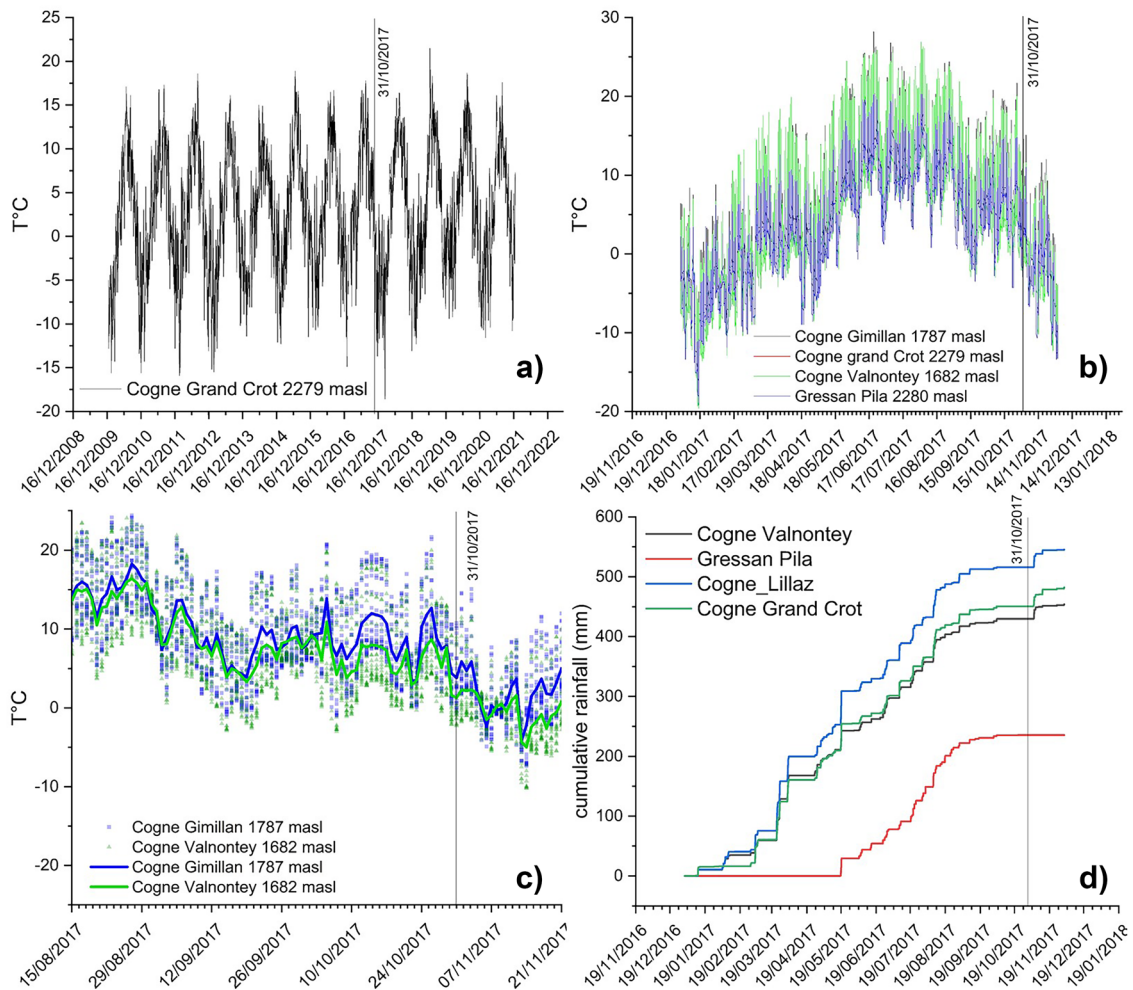


**Fig. 4** Temperature time series for some of the meteo-stations located close to the Pousset area (see Fig. 1): **(a)** 2010–2022 mean daily temperature time series for the Cogne Grand Crot showing a 0.17 °C/year increase; **(b)** 2017 hourly temperature time series for four meteo-stations; **(c)** hourly and mean daily temperature time series for the period of the rockfall events. A decreasing temperature (ca 1.2–1.6 °C/day) was observed in the week before the event. **(d)** 2017 cumulative rainfall

## Dust sampling and analysis

### Aspect of rock dust deposit in the field

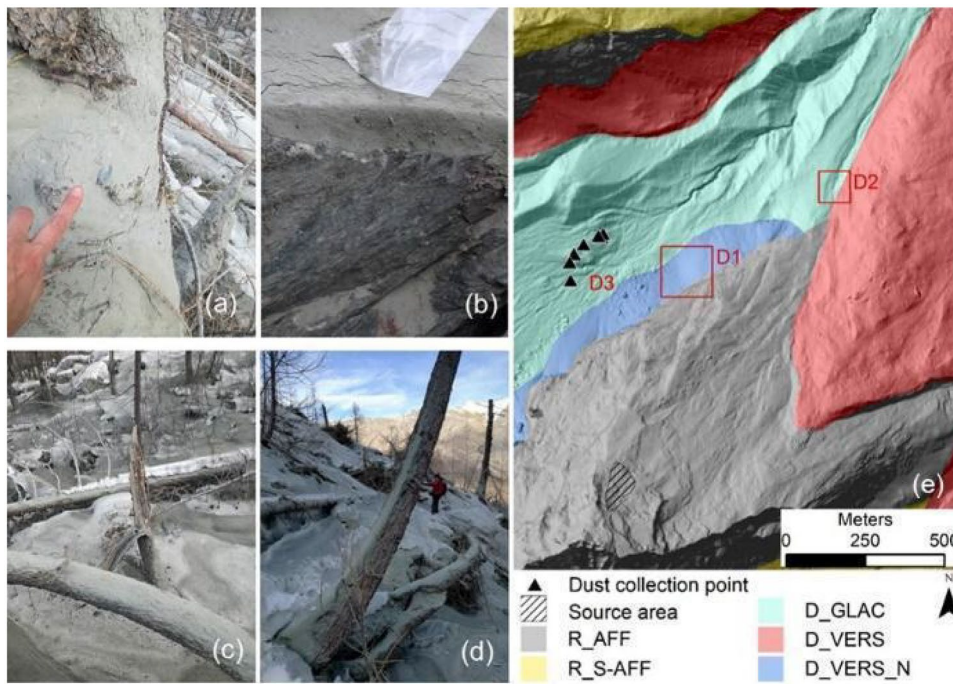
During the Pousset rockfall, a part of the rock volume was converted into a cloud of dust that settled close to the area of collapse and progressively along the path while traveling down to the main valley. The dust deposit thickness was measured and material was sampled, at different points around the collapse and main impact area (see Fig. 5) and in the main valley in November 2017.

Figure 5 shows the appearance of dust deposited on trees and rockfall boulders. The rock dust was still found perfectly in place and we were able to measure the thicknesses in different places and collect samples of the material from the ground, trees, and mountain hut structures. Note: (i) the conspicuous thickness of the deposit up to a few centimeters, decreasing with the distance from the center of the impact area (Fig. 5a) down to a thin film in the main valley and at the Epinel village (Fig. 1); (ii) a shielding

effect, i.e., the deposit is thicker on the upwind side of obstacles, which is particularly evident along the circumference of the tree trunks; (iii) the breaking of branches and trunks; (iv) the deposition both on horizontal and inclined surfaces (as tree trunks), indicating that deposition was not ruled only by gravitational settling, but also by the thrust by the dust cloud.

The rock dust was sampled and its thickness measured at seven different locations (Fig. 5). Furthermore, in the other three locations, we measured without sampling the dust thickness. Samples were collected from both loose (e.g., below trees or on mountain huts) and hardened (e.g., in the upper areas on trees and blocks) deposits and sealed in plastic bags for further examination in the laboratory.

Figure 6 shows the changing of the measured deposit thickness with distance from the main impact area and the experimental granulometric curves obtained from the previous considered samples compared with other granulometric curves obtained in analog cases.



**Fig. 5** High-density rock dust deposits on trees and large blocks at 2140–2150 m asl; (a) on the upwind side of a debarked tree trunk with some centimeter-sized elements immersed in a fine matrix; (b) on uprooted and snapped trees laying down in the direction of the cloud motion; (c) 3–4 cm thick and uniform dust layer on a rock block; (d) accumulation of the rock dust along the slope and trees in a position at about 2100 m asl; (e) map of the ground surface characteristics with the rockfall source area and the three main deposition zones (D1, D2, and D3) for the blocky material. Sampling points for the rock dust are also reported

Estimate of the rock dust volume from field measurement of deposit thickness

The amount of rock dust in the deposit was estimated as follows. The thickness  $T$  of the dust deposit is integrated as a function of the distance  $r$  from the main impact point

$$V_{dust} \approx \int_0^{\infty} 2\pi r T(r) dr \quad (1)$$

Assuming an exponential decrease  $T(r) \approx T_0 \exp(-\eta r)$  where  $\eta$  is the inverse of the decay length, in accordance with the trend shown in Fig. 6a, it follows that

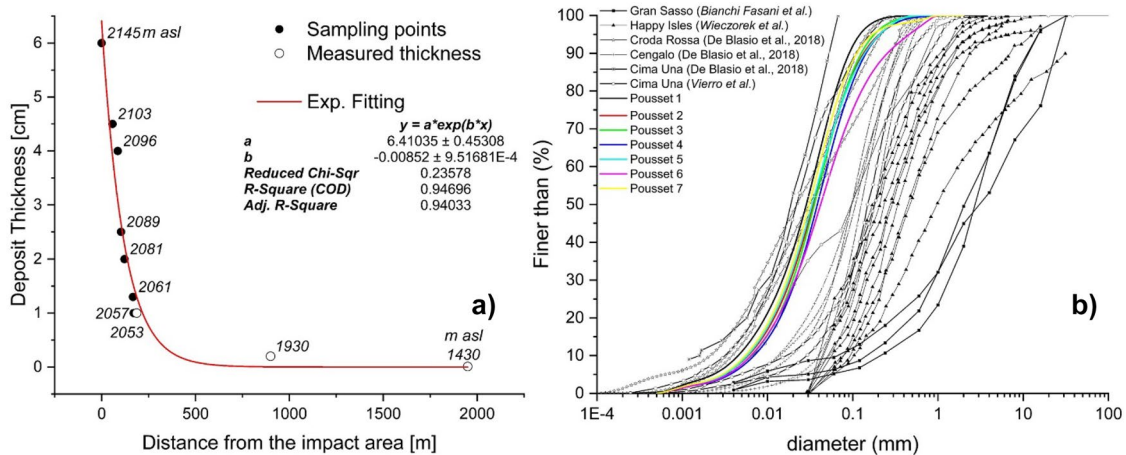


**Fig. 6** Characteristics of the dust layer at the Pousset site: (a) thickness versus distance from the main impact area measured on sub-horizontal surfaces; the sampling points are shown in Fig. 5 except for the ones at distance 900 m and 2,000 m, which are located further north-east. Furthermore, altitude of each sampling point is indicated; (b) grain size distribution of the seven samples collected between 2053 and 2145 m a.s.l (see Fig. 5) compared with those from other sites where EER events were observed and dust samples collected

$$V_{dust} \approx \frac{2\pi T_0}{\eta^2} \quad (2)$$

Figure 6a shows the exponential decay in dust thickness with the following fitting parameters:  $T_0 \approx 6.41035 \text{ cm}$  and  $\eta = 0.0852 \text{ m}^{-1}$ . Applying Eq. (2), the dust volume is  $V_{dust} \approx 55.49 \text{ m}^3$

This corresponds to an intact rock volume of about  $44.4 \text{ m}^3$  computed by assuming a dust layer void ratio  $e = 0.2$  by the equation  $V_{rock} \approx (1 - e)V_{dust}$ . Hence, the dust cloud included only a rock volume equal to about 0.6% of the initial rockfall volume.

### Grain size curves

The seven dust samples were analyzed via a Malvern Instruments Mastersizer 2000 particle size analyzer (measuring materials in the range 0.02 to 2000  $\mu\text{m}$ , based on Mie scattering principle) equipped with a Hydro 2000Mu large volume manual wet sample dispersion unit. Figure 6b shows the granulometric curves that are very similar to each other with a maximum difference between samples 1 and 7 represented by a shift in the grain size mode from 0.025 to 0.035 mm. The raw data shown in Fig. 6b tell us that 50% of the rock dust particles were finer than 0.025 mm, or 25 microns, and there was still an abundance of dust of size less than 10 microns. This indicates a very severe comminution, which is in line with other events recorded in the Alps (De Blasio et al. 2018). The data for Happy Isle Yosemite and the Gran Sasso (central Italy) rockfalls (Wieczorek et al. 2000; Bianchi Fasani et al. 2013; Viero et al. 2013) shown in Fig. 6b indicate coarser grains suggesting a less intense fragmentation or local effects (e.g., rock texture, lithology, fall trajectory).

### Rockfall simulation

The dynamics of the falling blocks was investigated by means of the HyStone rockfall simulator. HyStone is a 3D rockfall simulator code reproducing the block motion from the dynamics equations (Crosta et al. 2004; Frattini et al. 2012) and considering the topography of the region under study using the Digital Terrain Model (DTM). HyStone solves the equations of motion for a boulder traveling on the three-dimensional terrain by four basic processes: ballistic flight, bouncing along the flanks, sliding, and rolling. In the present case, the topography was described by means of a  $0.5 \text{ m} \times 0.5 \text{ m}$  DEM. Because of uncertainties regarding the initial block conditions and failure sequence, we ran the program for a different set of conditions including different initial velocities and positions.

In this section, we begin describing the HyStone rockfall simulation code. The aim of these simulations is the reproduction of the block trajectory and the computation of the impact points where a strong energy dissipation and block fragmentation is observed. In the successive section, the dust cloud motion is analyzed.

### HyStone code

Two types of analysis are possible with the HyStone code: lumped mass approach in which the block geometry is completely neglected by modeling the block as a material point, and the hybrid description where the block geometry is taken into account. The detailed model equations solved by HyStone are reported in the supplementary materials. When the blocks impact on the soil the code computes the bouncing velocity starting from the impacting

velocity and the chosen impact model. Four different types of impact models are implemented: (a) constant restitution approach, (b) restitution coefficient modified by impacting velocity, (c) restitution coefficient modified by the block mass, and, finally, (d) the elasto-visco-plastic rheological model. In the supplementary materials, a description of these equations is carried out. In the following HyStone analysis, for the sake of simplicity, we use the first model. To reproduce the uncertainties due to the natural variabilities, HyStone allows stochastic numerical analysis to be performed via a series of parameters PDFs (Frattini et al. 2012). The code is able to reproduce the fragmentation splitting up a block in fragments moving, after their separation, independently from each other. The fragmentation onset occurs when the energy criterion proposed by Yashima et al. (1987) is satisfied, i.e., the block fragments when its kinetic energy at impact overcomes the fragmentation energy  $E_{fr}$  estimated by using the Weibull parameter  $m_w$  as follows

$$E_{fr} = 0.15B_f C_f \left( \frac{1 - \nu^2}{E} \right)^{\frac{2}{3}} (2R_{bl})^{\frac{3m_w - 5}{m_w}} \left[ \sigma_0 V_0^{\frac{1}{m_w}} \right]^{\frac{5}{3}} \quad (3)$$

where  $E$  and  $\nu$  are Young's modulus and Poisson's coefficient, respectively,  $\sigma_0$  is the stress limit, and  $V_0$  is a representative volume. Finally, coefficients  $A_f$ ,  $B_f$ , and  $C_f$  are computed by means of the following expressions

$$A_f = \begin{cases} 0 & \text{if } m_w = 1 \\ \frac{5(m_w - 1)}{3m_w} & \text{otherwise} \end{cases} \quad (4)$$

$$B_f = \begin{cases} 1.0 & \text{if } m_w = 1 \\ \pi^{A_f} & \text{otherwise} \end{cases} \quad (5)$$

$$C_f = 6^{\frac{5}{3m_w}} \quad (6)$$

Once the fragmentation criterion is satisfied, the block is split up in fragments; the fragmentation algorithm computes the number and the size of fragments according to a power law distribution

$$G(D) = \left( \frac{D}{D_m} \right)^n \quad (7)$$

where  $D$  is the fragment diameter,  $D_m$  is the maximum fragment diameter,  $n$  is a model parameter controlling the shape of particle size distribution, and  $G(D)$  is the percentage of fragments finer than  $D$ . The maximum fragment diameter is proportional to the parent block diameter by means of a coefficient  $f_d$ . After the fragment generation, the velocity modulus of each fragment is computed under the hypothesis that the parent block translational kinetic energy is equally distributed to all fragments. Finally, the code imposes that the direction of the fragments velocity belongs to a cone whose apex coincides with the last impact point where the fragmentation took place. A fragmentation model parameter controls the apex angle of this cone. Experimental results have shown that block splitting (low energy Matas et al. 2017; Lin et al. 2020) and fragmentation (high energy) can affect the runout and the spatial distribution of velocities and heights of the rockfall.

## Model settings

The regional DTM available for the Aosta Valley has a  $0.5 \text{ m} \times 0.5 \text{ m}$  resolution allowing for a detailed description of the topography. As noticeable in Fig. 7, the propagation zone of the rockfall includes two main paths of which one characterized by a terminal 150–200 m high cliff before reaching the talus deposit (see profile P1 in Fig. 8). The rockfall source area extends for about  $8700 \text{ m}^2$  between 2730 and 2905 m asl. To simplify the simulation and evaluate the different controls, the source area was split in two subparts (see Fig. 8, upper and lower half), the number of launched blocks per cell was changed between 1 and 10, three block volumes were tested (i.e., 1, 3, or  $10 \text{ m}^3$ ), and fragmentation was in some simulation allowed and in others enabled (see Table S1 in supplementary material for a list of the performed simulations). A hybrid modeling approach was adopted to include the effect of block geometry, with normal and tangential restitution coefficients and the friction coefficient determined by slope material characteristics (Table 1) and successively calibrated and a stochastic range was assumed for each of them. On the contrary, the block density ( $2700 \text{ kg/m}^3$ ), launch translational and rotational velocities ( $1 \text{ m s}^{-1}$ ,  $1 \text{ s}^{-1}$ ), and the launch angle ( $10^\circ$ ) were kept constant.

## Rockfall simulation results

Two examples of the trajectories computed by neglecting blocks fragmentation in the calculations (SIM#01) or including

fragmentation (SIM#13) are reported in Fig. 7. The final block positions are also reported in the same figures. The three main clusters of arrest points (D1, D2, and D3) are visible and fit well with the distribution observed in the field (Fig. 5) with the D3 deposit area interested by a lower block frequency.

To classify the arrest points and main impact points (i.e., the most energetic and possibly associated to fragmentation), the analysis domain was split up in six sectors as shown in Fig. 8 where the stopping points are also reported.

These zones were outlined according to in situ investigations, morphological features, and the computed trajectories. The same figure shows the percentage of stopping blocks for each sector with respect to the total number of launched blocks. The majority of blocks belongs to sectors S1 (20.3%) and S2 (56.8%), while the remaining sectors account in total only for 22.9% of fallings blocks (Fig. 8).

Since in the fragmentation process the main controlling parameter is the maximum specific energy (i.e., the block energy at impact divided by the block mass), we plotted this quantity in Fig. 7. From the analysis of these impact points, two main macro-sectors were identified according to the different amount of energy dissipated. In coincidence with the deposit areas D1 and D3, the released energy (greater than  $1.0 \text{ kJ/kg}$  and up to more than  $3.0 \text{ kJ/kg}$ ) is greater than within the deposit D2 area (lower than  $1.0 \text{ kJ/kg}$ ). As shown in Fig. 8, deposits D1 and D3 occur below a high terminal cliff (profile P1), whereas deposit D2 is located at the end of an even and gentler slope (P2). In the same figure, the number of final blocks and

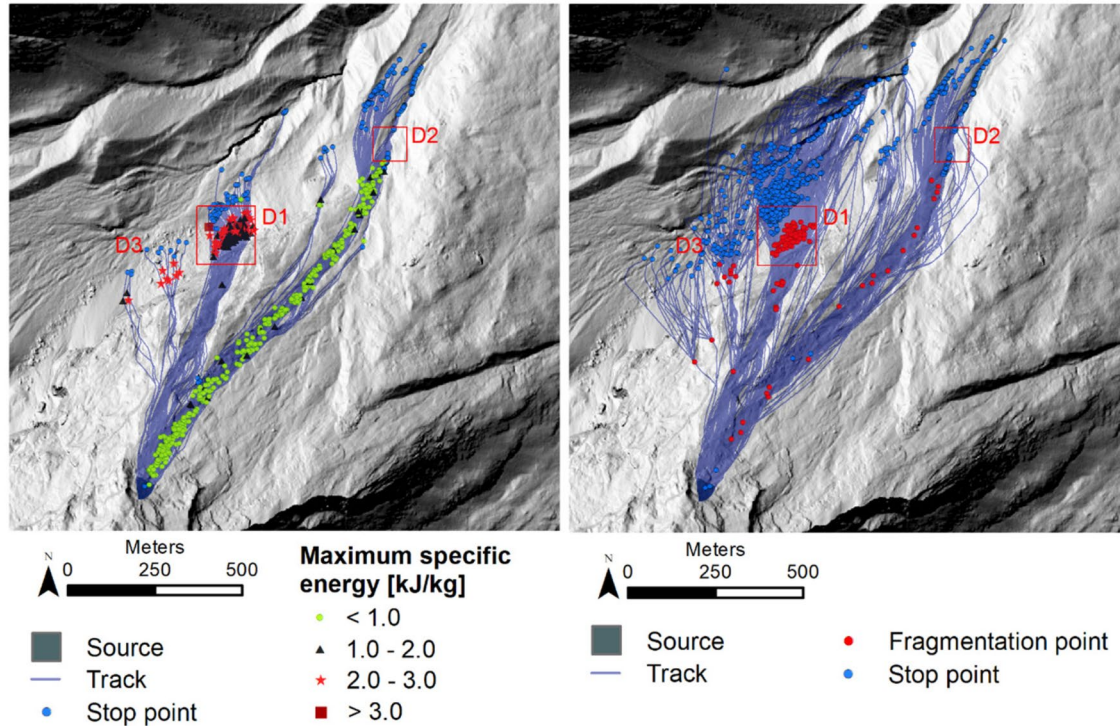


**Fig. 7** Simulated rockfall trajectories and arrest points for (a) SIM01, with disabled fragmentation, showing the maximum specific energy in four energy intervals. Points and values refer to the maximum specific energy calculated by analyzing each impact of each simulated trajectory; (b) SIM13 with fragmentation. The three main deposit areas D1, D2, and D3 are shown



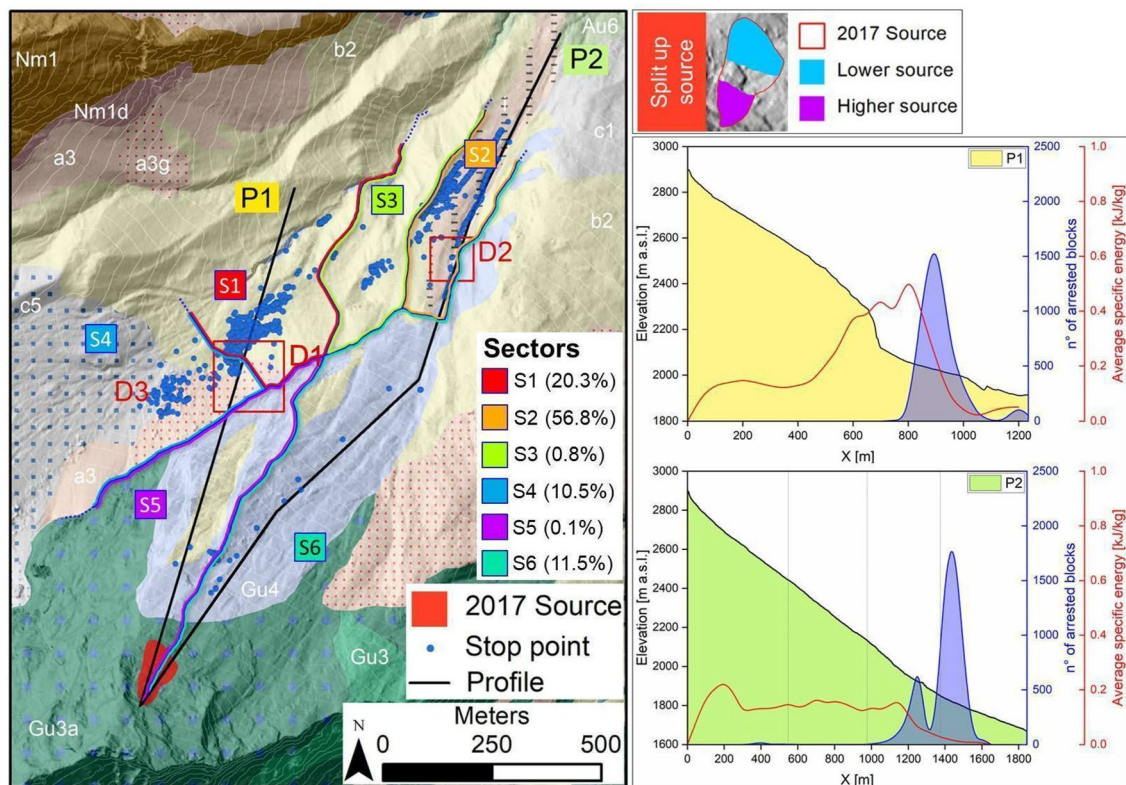


**Fig. 8** Numerical setting and altitude profiles of the preferential paths taken by blocks. In the right graphs, also the number of blocks comes to rest and of average specific energy along the two profiles is reported. The location of the three main deposits D1, D2, and D3, and the arrest points of simulated blocks in simulation SIM09 and the subdivisions of the domain in six sectors are also indicated. For each sector, the percentage of final blocks with respect to the total number of blocks (50,707) is reported. The 1:10,000 geological map of the area is labelled: i) mixed origin deposit, c5) ablation till, a1) landslide deposit, b2) colluvium, a3g) large boulders deposit, c1) unsorted till, a3) landslide debris, Gu4) calcschists, Gu3a) albitic amphibolites, Gu3) metabasites, Nm1) microcrystalline gneiss, Nm1d) quartz gneiss

the average specific energy extracted along the profiles indicate a single main deposit for P1 whereas a more distributed deposit for P2, and an increase in the average specific energy at the main cliff jump for P1.

Figure 9 shows the analysis of the maximum specific energy collected for each sector for simulation SIM#01, assumed as representative of all our simulations. The dashed lines in the graphs

identify the same energy classes (i.e., low, medium, and high energy). The high-energy class (i.e., values greater than 3.0) is reached only in sectors S1 and S4 (with a relative frequency lower than 0.2) at deposit areas D1 and D3. The medium-energy class is reached in all the sectors, except in the very densely populated sector S2. Notice that the calculated specific energies in the sectors 1, 3, and 4 are the highest of all possible paths, including many blocks of energy larger than 2000 J/kg. This corresponds to a free fall height of about 200 m. The energy threshold for fragmentation is shown in the same plot for three possible scenarios: a low-, medium-, and high-energy threshold. These values are approximately indicated by in situ experiments with large boulders dropped from a certain height.

Figure 10 shows the distance ranges between the impact point where the maximum dissipation occurs and the stopping point (box and whiskers plot) together with the maximum dissipation specific energy (histogram plots with dashed lines for distributions) for each sector. Apart sectors S5 and S6 where the blocks do not reach the terminal cliff, blocks experiencing the maximum values of dissipation energy (sectors S1 and S4) show the largest standard deviation and mean values. Specific energy dissipation values are greater for blocks belonging to sectors S1 and S4 confirming that these blocks can undergo fragmentation enhanced by presence of

**Table 1** Values of normal and tangential restitution coefficients and of the friction coefficient for the different slope materials used in the rockfall numerical simulations

Material denomination	$e_n[-]$	$e_t[-]$	$\mu_s[-]$
Glacial deposit	65	80	0.40
Slope debris	65	70	0.60
Bare slope debris	65	70	0.50
Alluvial deposit	55	60	0.40
Outcropping rock	85	85	0.30
Sub-outcropping rock	80	80	0.30

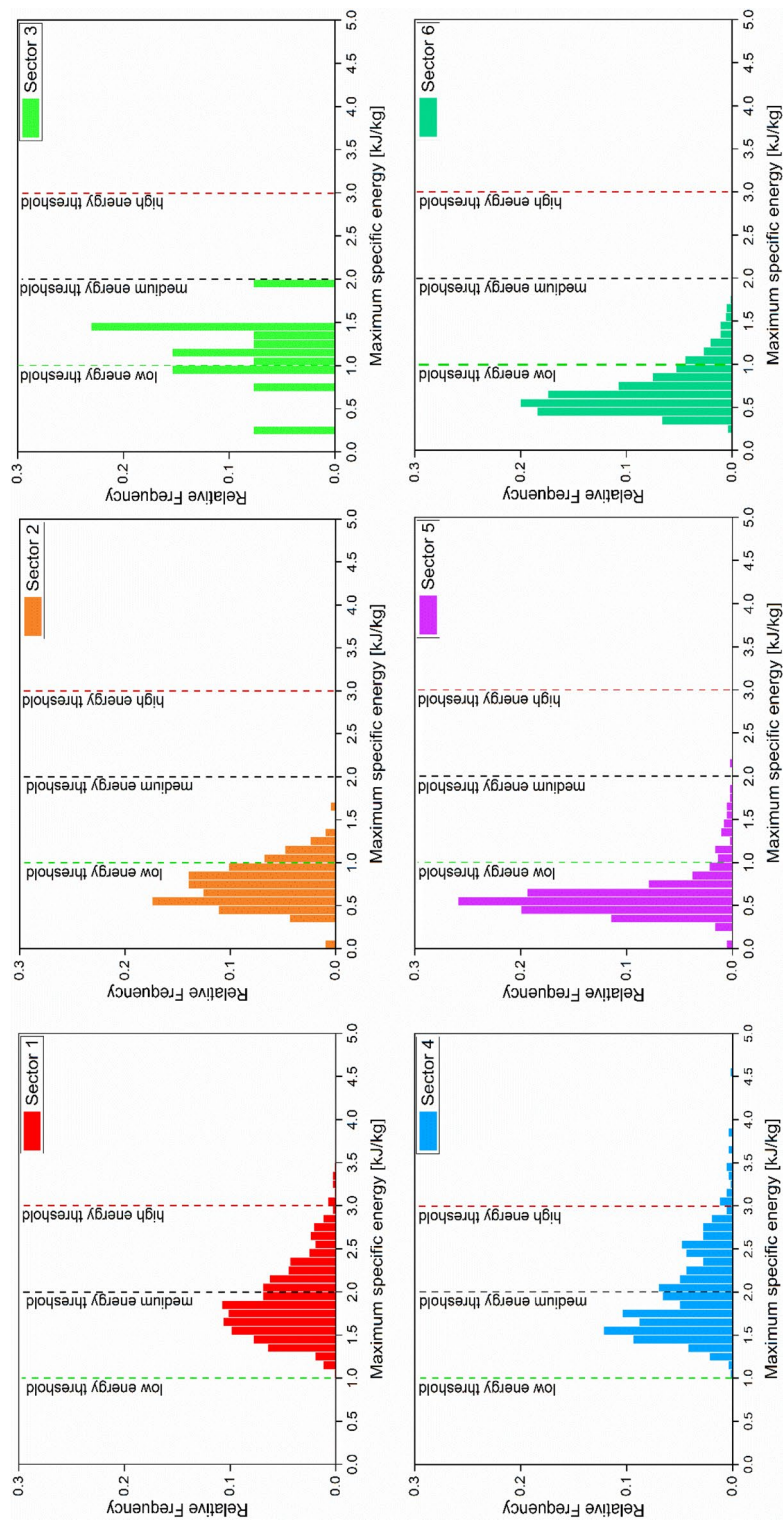


**Fig. 9** Histograms of maximum specific energy frequency distribution calculated for each one of the six sectors (see Fig. 8, colors as in the figure) in simulation SIM01. Vertical dashed lines identify low-, medium-, and high-energy threshold values

small precipice. In spite of this difference in energy dissipation, the blocks are capable of traveling a long distance but shorter than for those in sectors S2 and S3 where fragmentation was less severe.

According to these observations, the D1 and D3 areas are the more likely sources for the fragmentation and consequently for the formation of the dust cloud (see Fig. 3). As a partial verification of the results

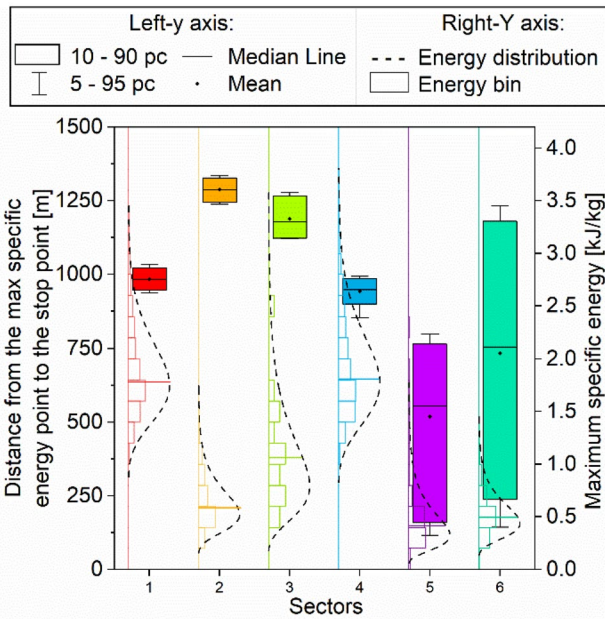


**Fig. 10** Box and whiskers plot of the distance between the impact point, where the maximum energy is dissipated, and the stopping point for the simulations SIM01; horizontal bar histograms refer to the maximum specific energy distribution. Data are analyzed for each one of the six sectors delineated in Fig. 7

obtained by HyStone for fragmentation, Fig. S 2 of the Supplementary material shows the characteristics of the deposits D1 and D2. In the D1 area, the fragments are finer than in deposits D2, confirming the severity of fragmentation in D1 as from calculations. Another feature supporting this conclusion is represented by tree abrasion observed in the D1 and that is completely absent in the deposit D2. Furthermore, the blocks in D1 are covered and embedded in a grayish powder that is a residual of the dust cloud formation.

### Dust cloud analysis

#### Fragmentation energy

A quantitative analysis of the various forms of energy dissipated by rockfall blocks at collapse was presented in De Blasio et al. (2018). The main energy dissipation processes are seismic waves, mass fragmentation, heat, kinetic energy of the fragments (responsible for the weak shock wave in the air), and acoustic energy. It was concluded that most of the initial EER energy goes into fragmentation of rock blocks and the kinetic energy of the fragments. In the following, the dust grain size data (Fig. 6) was used to estimate the fragmentation energy.

Using a series of functional forms to fit the granulometric curves, we found the best fit with the normalized Generalized Extreme Value (GEV), whose expression is

$$G(D) = \frac{(G_{Max} - G_{Min})g(D) - G_{Min}g(D_{Max})}{g(D_{Max})} \quad (8)$$

being  $G_{Max}$  and  $G_{Min}$  the passing percentages for the maximum and minimum diameters  $D_{Min}$  and  $D_{Max}$ , respectively, whereas  $g(D)$  is the following function

$$g(D) = \exp \exp \left\{ - \left( 1 + \xi \frac{D - \mu}{\sigma} \right)^{-\frac{1}{\xi}} \right\} - \exp \exp \left\{ - \left( 1 + \xi \frac{D_{Min} - \mu}{\sigma} \right)^{-\frac{1}{\xi}} \right\} \quad (9)$$

where  $\xi$ ,  $\mu$ , and  $\sigma$  are three model parameters.

Assuming that the clasts have spherical shape, with diameter ranging between  $D_{Min}$  and  $D_{Max}$ , the newly generated area for all clasts ( $S$ ) is

$$S_{sphere} = 6V_{dust} \int_{D_{Min}}^{D_{Max}} \frac{1}{D} \frac{dG}{dD} dD \quad (10)$$

In this equation, the perfect sphericity of the particles is a strong approximation that causes an underestimation of the generated surface, and consequently of the energy absorbed by fragmentation. For this reason, De Blasio et al. (2018) suggested the use of the sphericity index,  $s$  (i.e., the ratio between the surface area of a real particle and the area of a spherical particle of the same volume) for a better characterization of the grain surface and the quantification of the fragmentation energy. If the sphericity index remains constant (i.e., it is not a function of the particle size), then the surface produced is simply

$$S = \frac{6V_{dust}}{s} \int_{D_{Min}}^{D_{Max}} \frac{1}{D} \frac{dG}{dD} dD = \frac{S_{sphere}}{s} \quad (11)$$

Defining the fragmented fraction  $\eta_f$ , as the volume fraction of the initial rockfall volume that forms the dust cloud

$$\eta_f = \frac{V_{dust}}{V_b} \quad (12)$$

then the generated surface becomes

$$S = \frac{6\eta_f V_b}{s} \int_{D_{Min}}^{D_{Max}} \frac{1}{D} \frac{dG}{dD} dD. \quad (13)$$

The fragmentation energy,  $E_f$ , is given by the following expression

$$E_f = E_s S \quad (14)$$

where  $E_s$  is the fracture energy for unit surface, i.e., the energy cost to create a unit surface area.

The proposed approach to compute fragmentation energy is different from that normally employed in the comminution industry and its applications to rock avalanches. In the comminution industry, Bond's law is used to estimate fragmentation energy as explained in Appendix A (see also Rhodes 1998). Bond's law has been applied to estimate the energy sink of rock avalanches (Locat et al. 2006; Crosta et al. 2007; De Blasio and Crosta 2014) but it may be unsuitable when dealing with very small particles, for which other comminution laws such as von Rittinger's law (Rhodes 1998) were suggested. In contrast, von Rittinger's equation is not suitable for larger clasts and, consequently, no expression in literature considers the whole particle clast distribution. For this reason, we introduced the clast size distribution in the energy computation.

To calculate the fragmentation energy, von Rittinger's law was initially used assuming that the total fragmentation energy needed to bring an initially intact block to powder of a size spectrum  $G(D)$  is proportional to the surface created by fragmentation. In

this equation,  $D$  is a size which is conveniently fixed as the sieve opening size or, for digital granulometers, as the “representative” radius of the clasts. Hence, the energy absorbed by fragmentation is computed as

$$\Delta E = E_s \int_0^r G(r) S_c(r) dr \quad (15)$$

and  $S_c(r)$  is the surface of the clast of radius  $r$ . This is an ill-defined quantity, since there is no univocal relationship between  $r$  and  $S_c(r)$  as the clasts do not have all the same shape. In the following, we used the definition of the maximum particle diameter,  $D_{Max}$ , as the maximum length possible for a given geometry. Thus, the maximum size for a spherical and a cubic grain is the diameter  $S(r) = 4\pi r^2 = \pi D_{Max}^2$  and the diagonal  $2D_{Max}^2$ , respectively.

Because von Rittinger’s law was elaborated in the mining and comminution industry, it usually requires the starting size  $D(m)_{initial}$  of the feed (i.e., initial grain size) and that of the final product  $D(m)_{final}$ . Since the original expression is strictly dependent on the adopted units, we modified it proposing the expression

$$E_f \left( \frac{J}{kg} \right) = \frac{1}{\rho \left( \frac{kg}{m^3} \right)} E_s \left( \frac{J}{m^2} \right) \left( \frac{1}{D(m)_{final}} - \frac{1}{D(m)_{initial}} \right) \quad (16)$$

where  $D_{initial}$  and  $D_{final}$  are measured in meter,  $E_s$  is measured in  $\frac{J}{m^2}$ ,  $\rho$  is measured in  $\frac{kg}{m^3}$ , and, finally,  $E_f$  is measured in  $\frac{J}{kg}$ . Our Eq. (14) is more complete than (16) as it uses the “real” area produced by insertion of the particle size distribution  $G(D)$ .

The fragmentation energy for unit surface of an ideal solid consisting of one atomic species is easily estimated. When a new atomic area  $S_a$  is created within the solid, about  $N_a \approx \frac{S_a}{\pi a^2}$  atoms are separated, where  $a$  is the Wigner–Seitz radius (e.g., Kittel 1996), which for the present order-of-magnitude estimate is approximately the lattice spacing. Hence, the energy cost is  $E_{fa} = \frac{S_a \epsilon}{\pi a^2}$  where  $\epsilon$  is the energy needed to separate two atoms apart. This energy is smaller than the cohesive energy per atom (which accounts for the energy of interaction with all the other ions in the lattice), but it is typically of the same order of magnitude and will suffice for the present estimate; thus,

$$E_s \approx \frac{E_{fa}}{S_a} = \frac{\epsilon}{\pi a^2} \quad (17)$$

Cohesive energies are typically on the order of 1 eV per atom for alkalis, and some eV for more bound solids (Poole 1980). This amount would correspond to surface energies of  $\approx 1 \text{ J m}^{-2}$  that is the order of magnitude of surface energy measured for different minerals. For example,  $E_s = 1.27, 0.705,$  and  $0.548 \text{ J m}^{-2}$  for graphite, quartz, and average feldspar, respectively (Brace and Walsh 1962; Zhang and Ouchterlony 2022). Valero et al. (2011) report a higher value of  $E_s \approx 2\text{--}3 \text{ J m}^{-2}$  for quartz showing some divergence among literature data. Similarly, higher values were reported for alkali feldspars by Brace and Walsh (1962) and Atkinson and Meredith (1987):  $7.77 \text{ J m}^{-2}$  for orthoclase and  $3.20$  to  $5.25 \text{ J m}^{-2}$  for microcline. However, a rock is a polycrystalline material with different mineral species. The energy needed to separate two different grains along pre-existing boundaries is less than the one necessary to break through a well-formed crystal. For example, for anorthite,

the energy for unit of area necessary to produce an inter-granular crack is about  $2.74 \text{ J m}^{-2}$ , which dramatically reduces to  $0.55 \text{ J m}^{-2}$  if the crack develops between two crystals (Tromans and Meech 2002). A comparable reduction of the energy per unit area by a factor 4–5 was reported by Tromans and Meech (2002) from the case of crystal cracking to the one along crystal-crystal boundary). Furthermore, it can be expected that the fracture energy of rocks composed of more than one crystalline species will depend on the crystalline state (mono vs polycrystalline). Here, to be consistent with the few data available, we use a surface energy ranging between 0.1 and  $0.5 \text{ J m}^{-2}$ . Note that in the comminution industry, it is known that only about 5% of the energy expended in dedicated apparatuses goes into fragmentation with the rest going into other energy sinks (e.g., noise, heat, Rhodes, 1998).

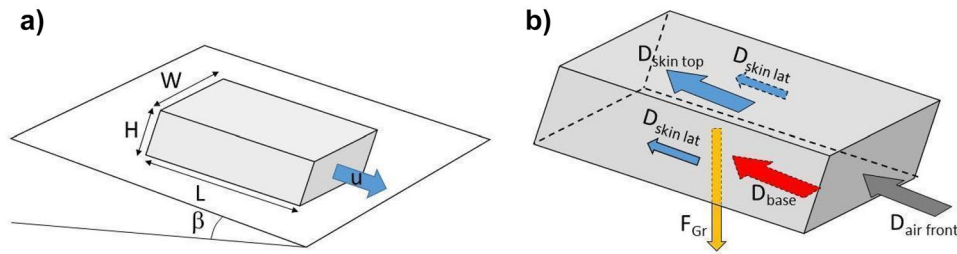
Table S 2 shows the parameter calibration of the lognormal particle size distribution (Eq. (16)) by means of the least square method together with the error of the estimation. To this purpose, the granulometric curves obtained from the seven samples collected at different locations (Fig. 6) were used. The curves fit very well the experimental data as suggested by the small error which reaches a maximum of 0.0019%.

Table S 3 shows the values of the generated particle surface area together with the fragmentation energy and the specific fragmentation energy (i.e., the fragmentation energy per unit volume). These computations are performed by considering the parameters of Table S 2 and considering the previously estimated  $V_{dust}$  value for  $\eta_f = 0.00965$ . The data reported in the first column of Table S 3 were calculated under the assumption that the whole failed mass of  $8000 \text{ m}^3$  had gone into the finest dust cloud component. Because only a fraction  $\eta_f \approx 0.00965$  of the rock mass was so intensely comminuted to generate a dust cloud, the total energy gone into fragmentation for the formation of the dust cloud should be multiplied by  $\eta_f$ . The last column of Table S 3 shows the resulting values. Note that the fragmentation energy per unit mass calculated from the dust size analysis (about  $10^4 \text{ J/kg}$  except for one sample giving values one order of magnitude larger) even exceeds the kinetic energy per unit mass available (in any case, less than  $4000 \text{ J/kg}$  as shown in Fig. 9). This indicates that the energy was focused on a small portion of the mass, which were so profoundly fragmented, while the rest of the colliding block was spared such severe fragmentation. This indicates that the rocky dust was produced in the front of a sacrificial layer of the colliding blocks.

A final remark is due regarding the rock area generated by fragmentation. It may appear surprising that areas produced by fragmentation are so large as reported in Table S 3. This can be explained by a simple order of magnitude estimate. The breakage of a cubic block of side length  $L$  and volume  $V$  into  $N$  small cubical grains of side  $l \ll L$  creates a total area  $\Delta A$  increment due to the fragmentation on the order

$$\Delta A \approx 6Nl^2 \approx 6 \left( \frac{L}{l} \right)^3 l^2 = \frac{6V}{l} \quad (18)$$

Using  $l \approx 10 \mu\text{m} = 10^{-5} \text{ m}$  and  $V \approx 8000 \text{ m}^3$ , it follows that  $\Delta A \approx 4.8 \times 10^9 \text{ m}^2 = 4.8 \times 10^3 \text{ km}^2$ , i.e., the same order of magnitude reported in our data. The maximum and minimum values obtained for the sample #1 and sample #4, respectively, were of the same order of magnitude. Calculations, considering the shape of the



**Fig. 11** (a) Dust cloud box used in the model with the cloud geometry and the ground surface sloping at an angle  $\beta$ ; (b) forces acting on the box of element (a): the gravity force ( $F_{Gr}$ ), the basal force slope-drag ( $D_{Base}$ ), the front air drag ( $D_{air front}$ ), and the skin-air force ( $D_{skin top}$ ,  $D_{skin lat}$ ) acts on the three lateral surfaces

clasts (Fig. 2), show that a plausible value for  $s$  could be substantially lower than 0.806 corresponding to cubical clasts, and we used  $s = 0.5$ .

### Dust cloud propagation

The aim of this section is the estimation of maximum speed and run out of the dust cloud. Particulates clouds are initially set in motion by the momentum transmitted to the air by the exploding rock mass when hitting the ground at high speed (De Blasio et al. 2018). The subsequent acceleration is driven by the density difference between the suspension and ambient air. In the simple model suggested here, the cloud is already fully formed in its prismatic shape of dimensions  $H$ ,  $W$ , and  $L$  as in Fig. 11. In our model, the density of the suspension is constant, while lateral flows are neglected. Furthermore, we assume that the cloud moves along a surface of constant slope  $\beta$  and the differences between the behavior of the cloud head and body (Simpson 1982; Bridge and Demicco 2008) are not considered. The cloud size and the forces acting on it are represented in Fig. 11.

To estimate the velocity of the dust cloud, we write Newton's equation for the center of mass of the cloud

$$V \left( \rho_c + \frac{1}{2} \rho_a \right) \frac{du}{dt} = (\rho_c - \rho_a) g \sin \beta V - F_D \quad (19)$$

where  $u$  is the velocity,  $\rho_c$  is the density of the dust cloud,  $\rho_a$  is the air density,  $g$  is the gravity acceleration,  $\beta$  is the slope angle, and  $V$  is the dust volume. The dust density is given by the following expression

$$\rho_c = (1 - e) \rho_s + e \rho_a \quad (20)$$

being  $\rho_s$  the particle material density,  $\rho_a$  air density under standard condition, and  $e$  air fraction.

The drag force  $F_D$  is due to the interaction of the dust cloud with the air and the ground surface. The drag force is approximated as

$$F_D = \frac{1}{2} \rho_a (C_{cf} HW + C_{cb} WL + C_{cs} WL + 2C_{cs} HL) u^2 \quad (21)$$

where  $C_{cf}$  is the front drag coefficient,  $C_{cs}$  is the drag skin coefficient, while  $C_{cb}$  is the drag bottom coefficient accounting for the friction between the cloud and the ground surface. By introducing the following global drag coefficient

$$C = \frac{C_{cf}}{L} + \frac{C_{cs}}{W} + \frac{C_{cs}}{H} + \frac{C_{cb}}{H} \quad (22)$$

the drag force becomes

$$F_D = \frac{1}{2} \rho_a C V u^2 \quad (23)$$

and the motion equation can be rewritten in the following form

$$\frac{du}{dt} = \frac{\rho_c - \rho_a}{\rho_c + \frac{1}{2} \rho_a} g \sin \beta - \frac{1}{2} \frac{\rho_a}{\rho_c + \frac{1}{2} \rho_a} C u^2 \quad (24)$$

Defining the two parameters  $k$  and  $\lambda$  as

$$k = 2 \frac{\rho_c + \frac{1}{2} \rho_a}{\rho_a} \cdot \frac{1}{C} \quad (25)$$

$$\lambda = \sqrt{k \frac{\rho_c - \rho_a}{\rho_c + \frac{1}{2} \rho_a} g \sin \beta} = \sqrt{\frac{2}{C} \frac{\rho_c - \rho_a}{\rho_a} g \sin \beta} \quad (26)$$

the above differential equation becomes

$$\frac{du}{dt} = \frac{\lambda^2}{k} - \frac{1}{k} u^2 \quad (27)$$

and by using the method of variable separation, and after some algebra, it becomes

$$\frac{\left( \frac{\lambda}{\sqrt{k}} + \frac{u}{\sqrt{k}} \right)}{\left( \frac{\lambda}{\sqrt{k}} - \frac{u}{\sqrt{k}} \right)} = e^{\frac{2\lambda t}{k}} \quad (28)$$

providing the solution as

$$u = \lambda \frac{\left( e^{\frac{2\lambda t}{k}} - 1 \right)}{\left( e^{\frac{2\lambda t}{k}} + 1 \right)} \quad (29)$$

This function is monotonically increasing from zero velocity to a finite maximum, called limit velocity  $u_l$ . By taking the limit for  $t \rightarrow +\infty$ , the limit velocity is  $\lambda$ .

The displacement of the cloud can be easily calculated by integrating the dust velocity as

$$d_c(t) = \int_0^t u(t') dt' = \lambda \int_0^t \frac{\left( e^{\frac{2\lambda t'}{k}} - 1 \right)}{\left( e^{\frac{2\lambda t'}{k}} + 1 \right)} dt = \lambda \int_0^t \tanh\left(\frac{\lambda t'}{k}\right) dt = k \ln \left[ \cosh\left(\frac{\lambda t}{k}\right) \right] \quad (30)$$

Figure 12 shows the evolution of the velocity and displacement of the dust cloud considering both Eqs. (29) and (30) using the parameters collected in the same figure and for three values of coefficient

$$d_c(t) = \int_0^t u(t') dt' = \lambda \int_0^t \frac{\left( e^{\frac{2\lambda t'}{k}} - 1 \right)}{\left( e^{\frac{2\lambda t'}{k}} + 1 \right)} dt = \lambda \int_0^t \tanh\left(\frac{\lambda t'}{k}\right) dt = k \ln \left[ \cosh\left(\frac{\lambda t}{k}\right) \right].$$

For all curves, the velocity increases with time reaching a limit value, which increases at reducing the coefficient  $C_{cb}$ . In particular, for a coefficient  $C_{cb} = 0.25$ , the maximum cloud velocity is about  $25 \text{ms}^{-1}$  and the maximum dust cloud displacement is 1.5 km which approximate the direct observations at the site (see Fig. 3).

### Cloud settling

During the cloud motion, particles tend to move downward due to the gravity action, but this vertical fall is contrasted by turbulence. Hence, for the sake of simplicity, we assumed that the cloud settling is more relevant for low velocities of the dust cloud. We also neglected the particle–particle interactions and the hindered settling (i.e., the action of the upward air movement in response to the vertical particle displacement) and we assume spherical particles. Under these assumptions, the particles are subject only to the gravity force and the air drag force which for small Reynolds number can be assumed to be Stokesian (Landau and Lifshitz 2013) so that the motion equation has the following form

$$m_p \frac{du}{dt} = m_p g - 6\pi\eta R_p u \quad (31)$$

in which  $m_p$  is the particle mass,  $u$  is the vertical component of the particle velocity,  $\eta$  is the air viscosity, and  $R_p$  the particle radius. By integrating the above differential equation, the following solution is obtained

$$u(t) = \frac{g}{\lambda} (1 - e^{-\lambda t}) \quad (32)$$

where  $\lambda$  is given by

$$\lambda = \frac{6\pi\eta R_p}{m_p} \quad (33)$$

and the particle displacement is obtained

$$d(t) = \frac{g}{\lambda} \left[ t + \frac{1}{\lambda} (e^{-\lambda t} - 1) \right] \quad (34)$$

If  $H$  is the dust cloud thickness, then the settling time (i.e., the time required to the particle to reach the ground surface) is obtained by imposing

$$d(t_s) = H \quad (35)$$

and the particle velocity at the soil is called the maximum velocity ( $u_{max}$ ) and is given by the velocity at  $t = t_s$ . The velocity function (Eq. (32)) is an increasing monotonic function that tends for  $t \rightarrow +\infty$  to the limit velocity  $u_l$  given by

$$u_l = \frac{m_p g}{6\pi\eta R_p} = \frac{2}{9} \frac{g \rho_s R_p^2}{\eta} \quad (36)$$

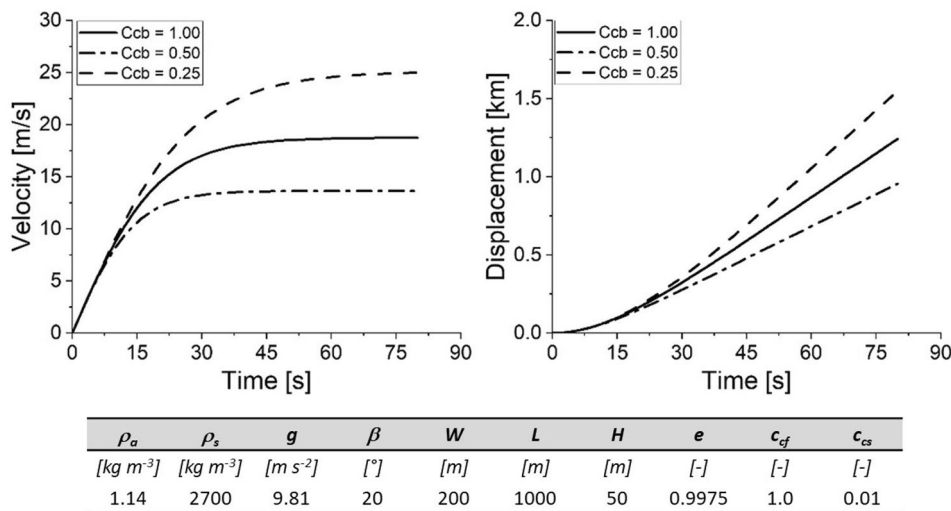
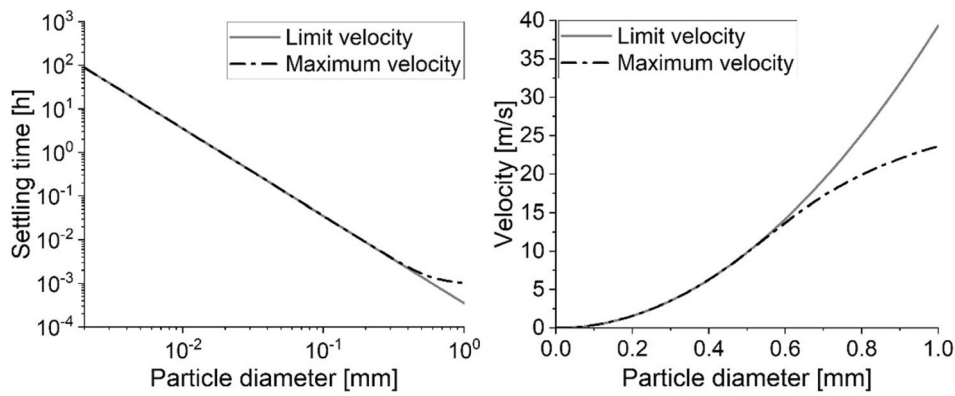
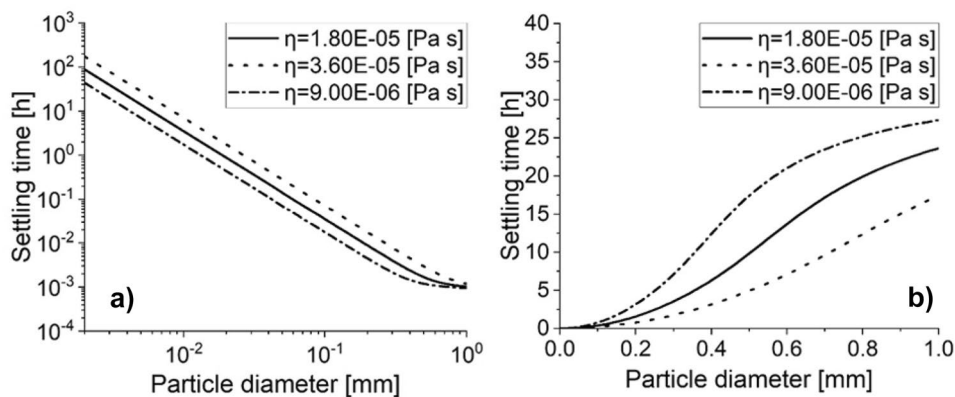


Fig. 12 Evolution of the cloud propagation (a) displacement and (b) velocity as a function of time calculated by Eq. (39). Three different values of the drag coefficients were considered. The values of the parameters employed in the computation are also reported



**Fig. 13** Settling time (a) and particle velocity (b) of the dust particles as a function of the particle diameter. The two curves are for a particle starting its fall at the limit velocity (continuous line) and for an accelerating particle (dash-dot line)



**Fig. 14** Parametric analysis of the air viscosity effect on the particle settling time and the velocity for different particle diameters

We define the limit settling time,  $t_{sl}$ , as the time required to the particle to settle starting its fall already at the limit velocity

$$t_{sl} = \frac{H}{u_l} = \frac{9}{2} \frac{\eta H}{g \rho_s R_p^2} \quad (37)$$

Using clean air dynamic viscosity value of  $\eta = 1.8 \cdot 10^{-5} \text{ Pa} \cdot \text{s}$ , and a dust cloud height  $H = 50\text{m}$  (i.e., a value comparable with the one observed in the propagation along the upper tributary valley, see Fig. 3), the evolution of the settling time and the limit settling time with particle diameter is represented in Fig. 12a. This computation shows that the settling time and the limit settling time in still air decrease with increasing particle diameter and the dust suspension of micrometric particles will persist for many hours. Obviously, this analysis neglects air current, winds, and the effect of air moisture that could contribute to clear the air in the area of interest. Furthermore, for small particles, the limit settling time and the settling time are coincident since small particles reach the limit velocity in short time in comparison with the settling time and consequently, it is possible to assume that these particles are at the beginning in the limit condition. The divergence between the settling time and the limit settling time increases with the particle diameters and for millimeter particles

the difference can be about one order. The above considerations are also confirmed by Fig. 13b where the limit velocity and the maximum velocity are represented in terms of particle diameters. By increasing the particle diameter, the differences between the limit velocity and the maximum velocity increases.

To study the effect of air viscosity, we performed a parametric analysis in which we have considered other two values of air viscosities. The obtained results in terms of settling time and maximum velocity are reported in Fig. 14. Independently from the air viscosity, an increment of particle diameter increases the maximum particle velocity and reduces the settling time. Note that an increment of the air viscosity increases the settling time and reduces the maximum particle velocity. Because the dust cloud is a mixture of particles with different class diameters (Fig. 6), large particles settle first leaving a haze of clay-size particles which, as our calculations confirm, may persist for several hours.

### Conclusions

Direct observations of the 2017 Pousset event and on-site investigation of the source, transport and deposition areas allowed us to reconstruct the dynamic of event and to collect useful information for a more in depth analysis. Apart from the large blocks delivered

at the base of the rocky cliff, most of the resulting clasts were found of millimeter-to decimeter size, and a fraction of the initial mass was comminuted to small particles of diameter between one micron to one-tenth of a millimeter. This last part was converted into a dust cloud that traveled along the tributary valley down to the main valley. The thickness of the dust deposit was measured, and found to decrease from the impact area. The estimated fraction of rock volume that ended up in the dust deposit was found to be about 45 m<sup>3</sup>, or 0.6% of the failed volume. Remarkably, the dust particles were found to be finer than in several EER events (or Extremely Energetic Rockfalls; De Blasio et al. 2018) which is surprising since EERs typically strike the ground with much higher energy per unit mass. It is possible that the impact energy was concentrated on a more localized area with the finest component of the dust produced by chipping of a sacrificial shell around the main failing block. The rest of the block enjoyed a buffering effect and was spared from such fine comminution. To verify such a condition, we simulated quantitatively the rockfall by the 3D HyStone code (Frattini et al. 2012; Crosta et al. 2015; Dattola et al. 2021) using a hybrid approach and including rock fragmentation. Simulations and direct observation both indicate that severe fragmentation occurred at two main impact points at the base of the cliff and these were the sources of the dust cloud. Fitting the particle size distribution, we found that the fragmentation energy per unit mass was about 10<sup>4</sup>–10<sup>5</sup> J/Kg, that is a small fraction of the available potential energy (about 10<sup>7</sup> J/Kg) was required to fragment 0.6% of the initial rockfall volume. In other words, relatively little energy went into the fragmentation of the rock mass. This is, however, the result of buffering by the sacrificial layer where a large amount of energy was used up in comminution.

The Pousset rockfall represents a controlled case to analyze since the different processes (rockfall, rolling, fragmentation, dust cloud propagation, dust cloud settling) can be examined one at a time. Still, many problems were addressed in a partial or approximated way, and should be more thoroughly considered in a future analysis of similar rockfall events. Firstly, the rockfall trajectories are based on some assumptions concerning the initial block size distribution and the fragmentation model (following Yashima et al. 1987). Secondly, the dynamics of fragmentation should be understood in a more complete theory based on physical analysis of crack propagation in the crystalline rock. In the present work, the fragmentation energy is simply proportional to the area created during fragmentation. Although this approach is expected to provide the correct order of magnitude, it nevertheless neglects the possibility of non-linear effects in fragmentation. It also overlooks the polycrystalline nature of rocks and the composition of different mineralogical species. Also, the microscopic dust has been treated as composed of particles with a definite shape. The deviation from sphericity (which gives a larger area for the given volume, and thus a larger fragmentation energy) is treated by introducing a sphericity parameter equal for all particles. More realistically, particles have complex shapes, and moreover, the ruggedness of their surface indicates a larger area of fragmentation and greater fragmentation energy. Thirdly, the dynamics of the dust cloud is treated with a simple mathematical model. In spite of its basic assumptions, the calculated velocities and the space traveled by the cloud are compatible with the observations as documented in the two videos of the Mount Pousset rockfall. We estimated a time needed for the dust cloud particles to settle ranging from some minutes to several hours for particles of different size.

As we documented, the rock dust particles span two–three orders of magnitude in size (i.e., six–nine in volume), which implies a differential settling. In addition, air properties like turbulent viscosity, air engulfment, and hindered settling should be properly introduced.

In the paper, we presented an analysis of the dust cloud deposit focused on the spatial thickness and granulometric distribution. Some potentially interesting features that for brevity were not reported require further investigations. In particular, the role of humidity could have played a role in the deposition and permanence of thick dust layers deposited on tree trunks that we found as hard as mortar. High velocity and compaction were relevant but also some moisture from water in the talus or from the scarred vegetation or from the air could be important. As a general outlook, it can be expected that during the occurrence of large rockfalls and rock avalanches, significant amounts of dust must have been produced. If a rapid deposition buried patches of the consequent dust layers during large prehistoric rockfalls and avalanches in the Alps, these could be still identifiable in some cases (Reznichenko et al. 2012). Hence, the investigation of these dust cloud layers for recent events may represent a valuable additional piece of information in the investigation of the dynamics of rockfalls and avalanches.

#### Acknowledgements

Videos of the Pousset rockfall are available at <https://www.youtube.com/watch?v=JnLsJBL1Uzs> and <https://www.youtube.com/watch?v=DqEIdmRLzbs&t=6s> (last accessed on February 2022).

#### Funding

Open access funding provided by Università degli Studi di Milano - Bicocca within the CRUI-CARE Agreement. The work was supported by CARIPLO 2016–0756—@RockHoRiZon—Advanced Tools for Rockfall Hazard and Risk zonation at the Regional Scale. The Ministry of University and Research is thanked for funding Project PRIN MIUR Urgent – Urban geology and geohazards: Engineering geology for safer, resilient and smart cities, 2017 HPJLPW. Progetto TECLA—Dipartimenti di Eccellenza, funded by MIUR partially supported this study.

#### Data availability

Data are available from the authors upon request.

#### Declarations

**Conflict of interest** The authors declare no competing interests.

**Open Access** This article is licensed under a Creative Commons Attribution 4.0 International License, which permits use, sharing, adaptation, distribution and reproduction in any medium or format, as long as you give appropriate credit to the original author(s) and the source, provide a link to the Creative Commons licence, and indicate if changes were made. The images or other third party material in this article are included in the article's Creative Commons licence, unless indicated otherwise in a credit line to the material. If material is not included in the article's Creative Commons licence and your intended use is not permitted by statutory regulation or exceeds the permitted use, you will need to obtain permission directly from the copyright holder. To view a copy of this licence, visit <http://creativecommons.org/licenses/by/4.0/>.



## Appendix A: HyStone motion equations

The HyStone code computes the block trajectories by splitting them in a succession of elementary motions: free fly, rolling, sliding and impacts/bouncing. Hereafter we illustrate the equation regarding these types of motions. Under the free fly condition the following ordinary differential equation is imposed:

$$m_{bl}\ddot{u} = m_{bl}g \quad (38)$$

where the  $m_{bl}$  is the block mass,  $u$  is the center of mass position vector, and  $g$  is the gravity field. For sliding condition the block velocity is obtained by imposing

$$\ddot{u} = g - f\hat{t} \quad (39)$$

where  $f$  is the friction coefficient and  $\hat{t}$  is the unit vector obtained normalizing the projection of block the velocity onto the sliding plane. The rolling motion is obtained by integrating the following equations

$$\{I_{bl}\ddot{\theta}_{y,me} = TR_{bl} - NbN = -m_{bl}g_{z,me}T = m_{bl}g_{x,me} - m_{bl}\ddot{x}_{me} \quad (40)$$

where  $\ddot{\theta}_{y,me}$  is the y-component of block angular velocity,  $N$  and  $T$  are the normal and tangential force components acting at the contact point, respectively.  $R_{bl}$  and  $I_{bl}$  are the block radius and its inertia moment, respectively,  $b$  is the tangential arm of the normal force which is used to introduce the rolling resistance,  $g_{x,me}$  and  $g_{z,me}$  are the x- and z- components of the gravity field components, and  $\ddot{x}_{me}$  is the x-component of the center of mass acceleration. All the vector components in the previous equations refer to the mechanical reference system, i.e. a reference system tangent to the slope with x-axis aligned to the motion direction.

When the impact process is concerned, HyStone has many different models comprising the constant and not-constant restitution coefficients (Pfeiffer and Bowen 1989) and the evolution of the elasto-visco-plasticelast-visco-plastic model initially proposed by di Prisco and Vecchiotti (2006) and extended to prismatic and blocks (Dattola et al. 2021). In this work, the hybrid approach was used with normal and tangential restitution coefficients depending on the normal velocity at impact. In particular, the normal velocity component is given by the following expression

$$\dot{u}_{za,me} = -\frac{e_n}{1 + \left(\frac{\dot{u}_{zb,me}}{D}\right)^2} \dot{u}_{zb,me} \quad (41)$$

where  $\dot{u}_{zb,me}$  is the z-component (normal direction in the mechanical reference system) of the block velocity before the impact,  $\dot{u}_z^{a,me}$  is the same but after the impact.  $D$  is a model parameter and  $e_n$  is the normal restitution coefficient depending only on the material properties. For tangential direction along y-axis the velocity components are null before and after since in the mechanical reference system y-axis is perpendicular to the block motion. Finally, the velocity components along x-axis are computed by means of the following expressions:

$$\dot{u}_{xa,me} \sqrt{\frac{T_1}{m_{bl}(R_{bl})^2 + I_{bl}}} \quad (42)$$

where  $\dot{u}_{xa,me}$  is the x-component of the block velocity after the impact, and  $T_1$  is computed as

$$T_1 = (R_{bl})^2 \left[ I_{bl} (\dot{\theta}_{yb,me})^2 + m_{bl} (\dot{u}_{xb,me})^2 \right] S_f F_f \quad (43)$$

where  $\dot{u}_{xb,me}$  is the velocity x-component of center of mass before the impact,  $\dot{\theta}_{yb,me}$  is the y-component of the angular velocity before the impact. Coefficients  $S_f$  and  $F_f$  are assessed by means of the expressions

$$S_f = \frac{e_t}{1 + \left(\frac{\dot{u}_{zb,me}}{C e_n}\right)^2} \quad (44)$$

and

$$F_f = e_t + \frac{1 - e_t}{B + \left(\dot{u}_{xb,me} - \frac{R_{bl}}{A} \dot{\theta}_{yb,me}\right)} \quad (45)$$

in which  $A, B$  and  $C$  are three model parameters,  $e_t$  is the tangential restitution coefficients depending on the material properties.

## Appendix B: Bond's law for fragmentation energy

Bond's law, is employed to calculate the energy consumption in comminution apparatuses, industrial mills and crushers (Rhodes 1998; King 2001). It has also been applied to rock avalanches (De Blasio 2005; Locat et al. 2006). The Bond work index  $W$  is defined as the energy necessary to disintegrate a unit mass of material from the top size  $D$  (that can be considered infinite in our problem) down to a particle size  $d$ . To account for the non-uniform distribution of particle size, the work index is conventionally set to the size diameter  $d_{80}$ , i.e., the particle diameter at which 80% of the particles have a diameter smaller than  $d_{80}$ . If  $d_{80}$  is measured in microns, the energy consumption per unit mass due to disintegration  $E_{DIS}$  is then (Rhodes 1998)

$$\frac{E_{DIS}}{M} = \frac{10W}{\sqrt{d_{80}(\mu m)}} \quad (46)$$

being  $M$  the parent block mass.

Using the grain distribution of the disintegrated rock in the aftermath of the Yosemite (Wieczorek et al. 2000),  $d_{80}(\mu m)$  is about 2,500 (or 2.5 mm), and with  $W = 60,000$  J/Kg for granitoid rock, it follows that  $E_{DIS}/M = 1.2104$  J/Kg. The fact that this is comparable or even higher than the energy per unit mass available shows that Bond's law is not useful when the particle size is much smaller than the typical final product of comminution machines, for which this formula is designed.

## References

- Atkinson BK, Meredith PG (1987) Theory of subcritical crack growth with applications to minerals and rocks. In: Atkinson BK (ed) Fracture mechanics of rock. Publ London, Academic Press, pp 111–166
- Bergomi MA, Dal Piaz GV, Malusà MG, Monopoli B, Tunesi A (2017) The Grand St Bernard-Briançonnais nappe system and the Paleozoic inheritance of the Western Alps unraveled by zircon U-Pb dating. Tectonics 36(12):2950–2972
- Bianchi-Fasani G, Esposito C, Lenti L, Martino S, Pecci M, Scarascia-Mugnozza G (2013) Seismic analysis of the Gran Sasso catastrophic rockfall (Central Italy). In: C Margottini et al (eds). Landslide science

- and practice, Vol. 6 [https://doi.org/10.1007/978-3-642-31319-6\\_36](https://doi.org/10.1007/978-3-642-31319-6_36). Springer Verlag Berlin Heidelberg
- Boeckli L, Brenning A, Gruber S, Noetzi J (2012) Permafrost distribution in the European Alps: calculation and evaluation of an index map and summary statistics. *Cryosphere* 6:807–820. <https://doi.org/10.5194/tc-6-807-2012>
- Brace WF, Walsh JB (1962) Some direct measurements of the surface energy of quartz and orthoclase. *Am Miner* 47(9–10):1111–1122
- Bridge J, Demicco R (2008) Earth surface processes, landforms and sediment deposits. Cambridge University Press
- Crosta GB, Agliardi F, Frattini P, Imposimato S (2004) A three dimensional hybrid numerical model for rockfall simulation. In: *Geophys Res Abstr* p 7962
- Crosta GB, Agliardi F, Frattini P, Lari S (2015) Key issues in rock fall modeling, hazard and risk assessment for rockfall protection. In *Engineering geology for society and territory-volume 2* (pp. 43–58). Springer, Cham.
- Crosta GB, Frattini P, Fusi N (2007) Fragmentation in the Val Pola rock avalanche, Italian Alps. *J Geophys Res: Earth Surface*, 112(F1)
- Dattola G, Crosta GB, di Prisco C (2021) Investigating the influence of block rotation and shape on the impact process. *Int J Rock Mech Min Sci* 147:104867
- De Blasio FV (2005) A simple dynamical model of landslide fragmentation during flow. *Landslides and Avalanches: ICFL 95–100*
- De Blasio FV, Crosta GB (2014) Simple physical model for the fragmentation of rock avalanches. *Acta Mech* 225(1):243–252
- De Blasio FV, Dattola G, Crosta GB (2018) Extremely energetic rockfalls. *J Geophys Res Earth Surf* 123:2392–2421. <https://doi.org/10.1029/2017JF004327>
- Di Prisco C, Vecchiotti M (2006) A rheological model for the description of boulder impacts on granular strata. *Géotechnique* 56:469–482. <https://doi.org/10.1680/geot.56.7.469>
- Frattini P, Crosta GB, Agliardi F (2012) Chapter 22- Rockfall characterization and modeling. *Landslides types Mech Model* 267
- Geertsema M, Clague JJ, Schwab JW, Evans SG (2006) An overview of recent large catastrophic landslides in northern British Columbia. *Canada Engineering Geology* 83(1):120–143. <https://doi.org/10.1016/j.enggeo.2005.06.028>
- Gruber S, Haeberli W (2007) Permafrost in steep bedrock slopes and its temperature-related destabilization following climate change. *J Geophys Res* 112, F02518.
- Gruber S, Hoelzle M, Haeberli W (2004) Permafrost thaw and destabilization of Alpine rock walls in the hot summer of 2003. *Geophys Res Lett* 31:L13504
- King RP (2001) Modeling and simulation of mineral processing systems. Butterworth Heinemann, Boston
- Kittel C (1996) Introduction to solid state physics, 7th edn. Wiley, New York
- Landau L D, Lifshitz EM (2013) Fluid mechanics: Landau and Lifshitz: course of theoretical physics Volume 6 (Vol. 6). Elsevier
- Lin Q, Cheng Q, Li K, Xie Y, Wang Y (2020) Contributions of rock mass structure to the emplacement of fragmenting rockfalls and rockslides: insights from laboratory experiments. *J Geophys Res: Solid Earth* 125(4), e2019JB019296.
- Locat P, Couture R, Leroueil S, Locat J, Jaboyedoff M (2006) Fragmentation energy in rock avalanches. *Can Geotech J* 43:830–851
- Malusà M, Polino R, Martin S (2005) Alpine-tectono-metamorphic evolution of the Gran San Bernardo nappe (Western Alps): constraints from the Grand Nomenon unit of the Zona Interna. *Bull Soc Géol France* 176:417–431
- Malusà MG, Faccenna C, Baldwin SL, Fitzgerald PG, Rossetti F, Balestrieri ML, Piromallo C (2015) Contrasting styles of (U) HP rock exhumation along the Cenozoic Adria-Europe plate boundary (Western Alps, Calabria, Corsica). *Geochem, Geophys, Geosyst* 16(6):1786–1824
- Malusà MG, Polino R, Zattin M (2009) Strain partitioning in the axial NW Alps since the Oligocene. *Tectonics* 28(3)
- Matas G, Lantada N, Coromina J, Gili JA, Ruiz-Carulla R, Prades A (2017) RockGIS: a GIS-based model for the analysis of fragmentation in rockfalls. *Landslide*
- Morrissey MM, Savage WZ, Wieczorek GF (1999) Analysis of the 1996 Happy Isles event in Yosemite National Park. *J Geophys Res* 104(B10):23189–23198
- Paranunzio R, Laio F, Chiarle M, Nigrelli G, Guzzetti F (2016) Climate anomalies associated with the occurrence of rockfalls at high-elevation in the Italian Alps. *Nat Hazards Earth Syst Sci* 16(9):2085–2106. <https://doi.org/10.5194/nhess-16-2085-2016>
- Pfeiffer TJ, Bowen TD (1989) Computer simulation of rockfalls. *Bull - Assoc Eng Geol* 26:135–146
- Phillips M, Wolter A, Lüthi R, Amann F, Kenner R, Bühler Y (2017) Rock slope failure in a recently deglaciated permafrost rock wall at Piz Kesch (Eastern Swiss Alps), February 2014. *Earth Surf Proc Land* 42(3):426–438
- Polino R, Bonetto F, Carraro F, Gianotti Franco, Gouffon Y, Malusà MG, Martin S, Perello P, Schiavo A (2015). Note illustrative CARG Foglio 090 Aosta della Carta Geologica d'Italia. 1–144.
- Poole RT (1980) Cohesive energy of the alkali metals. *Am J Phys* 48(7):536–538. <https://doi.org/10.1119/1.12056>
- Ravanel L, Allignol F, Deline P, Gruber S, Ravello M (2010) Rock falls in the Mont Blanc Massif in 2007 and 2008. *Landslides* 7:493–501. <https://doi.org/10.1007/s10346-010-0206-z>
- Ravanel L, Magnin F, Deline P (2017) Impacts of the 2003 and 2015 summer heatwaves on permafrost-affected rock-walls in the Mont Blanc massif. *The Science of the Total Environment* 609:132–143. <https://doi.org/10.1016/j.scitotenv.2017.07.055>
- Reznichenko NV, Davies TR, Shulmeister J, Larsen SH (2012) A new technique for identifying rock avalanche-sourced sediment in moraines and some paleoclimatic implications. *Geology* 40(4):319–322
- Rhodes M (1998) Introduction to particle technology. Wiley, Chichester
- Simpson JE (1982) Gravity currents in the laboratory, atmosphere, and ocean. *Annu Rev Fluid Mech* 14(1):213–234. <https://doi.org/10.1146/annurev.fl.14.010182.001241>
- Tromans D, Meech JA (2002) Fracture toughness and surface energies of minerals: theoretical estimates for oxides, sulphides, silicates and halides. *Miner Eng* 15:1027–1041 [https://doi.org/10.1016/S0892-6875\(02\)00213-3](https://doi.org/10.1016/S0892-6875(02)00213-3)
- Valero A, Valero AI, Cortés C (2011) Exergy of comminution and the crepuscular planet. In *Proceedings of the 6th Dubrovnik Conference on Sustainable Development of Energy Water and Environmental Systems*, Dubrovnik, Croatia, September, 25–29.
- Viero A, Furlanis S, Squarzone C, Teza G, Galgaro A, Gianolla P (2013) Dynamics and mass balance of the 2007 Cima Una rockfall (Eastern Alps, Italy). *Landslides* 10:393–408
- Walter F, Amann F, Kos A, Kenner R, Phillips M, de Preux A et al (2020) Direct observations of a three million cubic meter rock-slope collapse with almost immediate initiation of ensuing debris flows. *Geomorphology* 351:106933
- Wieczorek GF (2002) Catastrophic rockfalls and rockslides in the Sierra Nevada, USA. In: *Catastrophic landslides: Effects, Occurrence, and Mechanisms*. The Geological Society of America, S.G. Evans and J.V DeGraff (eds.), pp. 165–190.
- Wieczorek GF, Snyder JB, Borchers JW, Reichenbach P (2007) Staircase falls rockfall on December 26, 2003, and geologic hazards at Curry Village, Yosemite National Park, California: U.S. Geological Survey Open-File Report 2007–1378, available @ <http://pubs.usgs.gov/of/2007/1378/>. Paper presented at the 1st North American Landslide Conference, Vail, Colorado June 3–8, 2007
- Wieczorek GF, Snyder JB, Waitt RB, Morrissey MM, Uhrhammer RA, Harp EL, Norris RD, Bursik MI, Finewood LG (2000) Unusual July 10, 1996, rock fall at Happy Isles, Yosemite National Park, California. *GSA Bull* 112:75–85
- Yashima S, Kanda Y, Sano S (1987) Relationships between particle size and fracture energy or impact velocity required to fracture as estimated from single particle crushing. *Powder Technol* 51:277–282
- Zhang ZX, Ouchterlony F (2022) Energy requirement for rock breakage in laboratory experiments and engineering operations: a review. *Rock Mech Rock Eng* 55:629–667. <https://doi.org/10.1007/s00603-021-02687-6>

Supplementary Information The online version contains supplementary material available at <https://doi.org/10.1007/s10346-023-02115-6>.

**Giovanni B Crosta · Giuseppe Dattola · Camilla Lanfranconi · Fabio V De Blasio** (✉) · **Marco Malusà**

Università degli Studi di Milano Bicocca, Department of Earth and Environmental Sciences, Milan, Italy

**Fabio V De Blasio**

Email: fabio.deblasio@unimib.it

**Davide Bertolo**

Regione Valle d'Aosta, Dipartimento programmazione, risorse idriche e territorio, Aosta, Italy